# Nitric oxide formation in lean, methane-air stagnation flames at supra-atmospheric pressures

Philippe Versailles[a,b,*], Antoine Durocher[a], Gilles Bourque[a,b], Jeffrey M. Bergthorson[a]

[a]*McGill University, 817 Sherbrooke Street West, Montréal H3A 0C3, Canada*
[b]*Siemens Canada Limited, 9545 Chemin de la Côte-de-Liesse, Dorval H9P 1A5, Canada*

## Abstract

Increasingly stringent regulations are imposed on nitric oxide (NO) due to its numerous, direct and indirect, deleterious effects on human health and the environment. A better control of the post-flame temperature field to contain the thermal (Zel'dovich) route resulted in significant reductions of engine emissions. An improved knowledge of the chemistry and rate of the secondary prompt, NNH, and $N_2O$ pathways is now required to decrease nitric oxide emissions further. For this effort, NO laser-induced fluorescence (LIF) measurements are presented for lean ($\phi = 0.7$), jet-wall, stagnation, premixed flames at pressures of 2, 4, and 8 atm. For all cases, the NO-LIF signal increases rapidly through the flame front, and relatively slowly in the post-flame region where the temperature is too low to sustain the thermal pathway. Nitric oxide mole fractions are inferred from the measurements and show that the pressure has a very weak adverse effect on NO formation. Reaction pathway analyses are applied to flame simulations performed with

*Corresponding author:
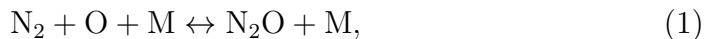Email address:* `philippe.versailles@mail.mcgill.ca` (Philippe Versailles)

a thermochemical model capturing the general trends of the data to assess the contribution of each NO formation route. For all cases, the $N_2O$ pathway, which proceeds mostly in the flame front region, dominates. This route produces slightly larger amounts of NO at higher pressures, but the variation appears very limited when considering the termolecular nature of its initiation reaction. The thermal route is predicted to progress slowly in the post-flame region, which causes a shallow increase in the NO mole fraction. The NNH and prompt pathways generate small amounts of NO, and their contributions reduce with the pressure. Overall, the thermochemical model predicts that the formation of NO is relatively unaffected by the pressure, which is consistent with the experiments. The experimental dataset reported in this work is made available for the development of thermochemical models.

*Keywords:*   High pressure, Laser-induced fluorescence, Nitric oxide formation, Particle Tracking Velocimetry, Stagnation flames

## 1. Introduction

Nitric oxide (NO) is a primary pollutant emitted by combustion-based devices that leads to the formation, in the atmosphere, of a variety of secondary pollutants, such as fine aerosols, acid precipitations, ground-level ozone, smog, and nutrient pollution of surface water, affecting human health and the environment [1]. To meet the ever-decreasing emission standards, engine manufacturers must develop new combustion chamber architectures [2]. To date, the main strategy has been to reduce post-flame temperatures to mitigate the rate of formation of nitric oxide through the thermal (Zel'dovich) route [3]. In the stationary gas turbine industry, the lean, premixed configuration received much attention and achieved $NO_x$ emissions below 10 ppm [4], a level where the $N_2O$, prompt, and NNH pathways are suspected to significantly contribute to the formation of nitric oxide [5]. However, the chemistry and rate of these production channels are not as well understood as for the thermal pathway. It is, therefore, necessary to assemble a wide set of independent experimental targets to properly constrain and validate the thermochemical models used as design tools, and to deepen the current understanding of the nitrogen chemistry. To minimize combustor-specific effects, these investigations must be performed in fundamental, laboratory burners [2].

The $N_2O$ pathway is made of an initiation reaction followed by two reactions producing nitric oxide [6, 7]:

$$N_2 + O + M \leftrightarrow N_2O + M, \tag{1}$$

$$N_2O + O \leftrightarrow NO + NO, \tag{2}$$

3

and,

$$N_2O + H \leftrightarrow NO + NH. \tag{3}$$

The termolecular reaction (1) is expected to progress more rapidly at high pressures, favouring the production of nitric oxide through the $N_2O$ pathway, which simulations suggest should be dominant in lean, premixed flames [7, 8]. While there have been some studies on NO formation in premixed flames of hydrocarbons at elevated pressures, using McKenna [9–12] and counterflow [13] burners, further investigations where the flame is minimally impacted by the burner surfaces, and providing accurate boundary conditions for thorough model validation, are needed.

The objectives of this paper are to quantify the effect of the pressure, $P$, on the formation of nitric oxide in lean flames, as well as to assess the relative importance of the $N_2O$ pathway at high pressures. LIF measurements of NO concentrations ([NO]) in lean ($\phi = 0.7$), premixed, jet-wall stagnation flames of methane and air at pressures of 2, 4, and 8 atm are presented. As described in section 2, the experiments are conducted in a recently commissioned high-pressure, laminar flame facility [14]. Flow velocity and NO concentration are sampled using Particle Tracking Velocimetry (PTV) and Two-Dimensional Planar Laser-Induced Fluorescence (2D-PLIF), respectively. The experimental data are presented in section 4, and used to verify the accuracy of a thermochemical model in predicting the flame reactivity, position, and NO formation. Reaction path analyses (RPA) are applied to the solution of flame simulations performed with an improved version of the model to estimate the fraction of NO molecules produced through the thermal, prompt, NNH, and $N_2O$ pathways, and to assess the effect of

4

the pressure on the nitrogen chemistry. The boundary conditions required for flame simulations are provided for the data to serve as validation targets for the development of thermochemical models.

## 2. High-pressure, jet-wall stagnation flame facility

The experiments are performed in a jet-wall stagnation burner, a geometry widely used to study the reactivity of flames, as well as the production of pollutants and their precursors [15–19]. This configuration provides compact, stable, lifted flames minimally affected by the burner boundaries, such that the measured reactivity, temperature, and species concentrations are sole functions of the properties of the reactant mixture.

The jet-wall stagnation burner employed for the current experiments is shown in Fig. 1. It is installed in an enclosure equipped with two pairs of sapphire glass windows for laser-based diagnostics. The geometry of the burner was optimized to provide laminar flames at high pressures [14, 20]. The combustible mixture exits the inner nozzle with a throat diameter of 10.2 mm, and impinges on the water-cooled stagnation plate located $\sim 9$ mm downstream of the nozzle assembly. The plate is maintained at temperatures below $\sim 445$ K to prevent surface reactions. The flame, shrouded by a co-flowing stream of nitrogen gas, stabilizes at the axial location where its speed balances the flow velocity.

The temperatures of the plate and the combustible mixture are sampled throughout the experiments with type-K thermocouples. Thermal mass flow controllers, calibrated with a dry-piston calibrator, monitor the fuel, air and inert streams. The pressure in the vessel is regulated by a digital controller
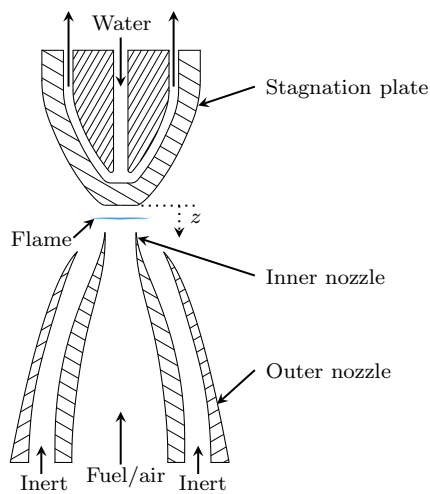
5

Figure 1: Jet-wall stagnation burner.

calibrated with a NIST traceable gauge, and coupled to a pneumatic valve.

The burner was designed to conform to the assumptions of the hydrodynamic model of Kee et al. [21] included in Cantera 2.3 [22]. It is based on an axisymmetrical stream function which, when assuming one-dimensionality of the axial velocity, temperature, species mole fraction, and density fields, allows to simplify the three-dimensional continuity, Navier-Stokes, and energy and species conservation equations to a quasi-one-dimensional formulation. The experimentally determined boundary conditions (BC) are reported in Table S1 of the supplemental material online. Namely, as prescribed in [23], the velocity boundary conditions are extracted from a least-squares parabolic fit to the data upstream of the flame measured using Particle Tracking Velocimetry [14, 24]. The simulations include the mixture-average formulation of the transport coefficients, as well as radiative heat losses. They are converged to absolute and relative tolerance levels of $10^{-9}$ and $10^{-5}$, respectively,

6

on grids refined to achieve gradient and curvature parameters of 0.05 and 0.075, respectively ($\sim$ 250 grid points).

Refractory particles seeded for laser-based velocity measurements do not exactly track high-gradient, high-curvature, chemically reactive flows due to the thermophoretic force and inertia. To account for the particle lag, the simulations are processed with the model of Bergthorson and Dimotakis [25] that applies Newton's second law to a virtual particle, recovers its trajectory, and computes the finite-difference scheme of the PTV method. This allows numerical and experimental profiles of particle velocity, $u_{\mathrm{p}}$, to be directly compared.

## 3. NO Laser-induced fluorescence

Nitric oxide formation is measured through two-dimensional, planar laser-induced fluorescence. The third harmonic of a Nd:YAG laser (Spectra-Physics Quanta-Ray Pro-230) pumps a wavelength-tunable dye laser (Sirah Cobra-Stretch SL) filled with a solution of Coumarin 450 dye. Ultraviolet light is obtained by passing the beam through a beta barium borate doubling crystal. Fused-silica lenses shape the beam into a $\sim$ 9 mm tall, $\sim$ 1 mm wide, sheet. The laser wavelength, $\lambda$, is adjusted to the spectral feature at $\sim$ 226.03 nm comprising the $S_{21}(4.5)$, $P_1(23.5)$, $P_{21} + Q_1$ (14.5), and $Q_2 + R_{12}$ (20.5) transitions in the A-X (0,0) electronic system of NO [26]. Combined with red-shifted detection, this was shown to provide the highest NO-LIF intensities, while minimizing interference from $O_2$-LIF [27]. The photons are collected by an ultraviolet, achromatic lens (Sodern Cerco 2178) mounted on extension tubes for improved magnification. It is equipped with a long-pass

7

filter (Semrock LP02-224R) that rejects most of the Rayleigh scattering and reflections from the burner surfaces, while transmitting the A-X (0,1) and subsequent vibrational emission bands of NO. Fluorescence images exposed for 300 ns, and binned 4 (vertically) by 8 (horizontally), are recorded with a monochromatic, 12-bit, intensified CCD camera (Dicam Pro, Gen II S-20 photocathode).

As shown in Eq. (4), the signal recorded by the camera, $S_{\mathrm{Raw}}$, is the combination of 1) the NO-LIF intensity, $S_{\mathrm{NO}}$; 2) a collection of interfering signals dependent on the laser energy, $S_{\mathrm{Bkg_1}}$ (*e.g.*, $O_2$-LIF, $CO_2$-LIF, and scattering) [27]; and 3) an irradiance independent background signal, $S_{\mathrm{Bkg_0}}$, mainly made of the camera dark noise and flame chemiluminescence. LIF in the linear regime, confirmed via comparison of experimental and numerical excitation spectra, is invoked to develop Eq. (5), where $F_i$ is the signal per unit laser energy. $S_{\mathrm{Raw}}$ and $S_{\mathrm{Bkg_0}}$ (without laser irradiation) correspond to an average of 5,000 and 2,000 images, respectively, and $E_{\mathrm{L}}$ is the mean of the time-integrated laser pulse power profiles measured with a high-speed photodiode (Thorlabs DET10A) and a 1 GHz sampling rate oscilloscope (Picoscope 2207B). One-dimensional profiles of $F_{\mathrm{NO}}$ are obtained by averaging the signal of 20 pixels ($\sim 4.2$ mm) around the axis of the burner at each axial position. The measurements are also corrected for local variations in the laser sheet intensity based on the average of 2,000 LIF images collected in a non-reacting 300 ppm NO / $N_2$ flow.

$$S_{\mathrm{Raw}} = S_{\mathrm{NO}}(E_{\mathrm{L}}) + S_{\mathrm{Bkg_1}}(E_{\mathrm{L}}) + S_{\mathrm{Bkg_0}} \qquad (4)$$

$$\frac{S_{\mathrm{NO}}}{E_{\mathrm{L}}} = F_{\mathrm{NO}} = \frac{S_{\mathrm{Raw}} - S_{\mathrm{Bkg_0}}}{E_{\mathrm{L}}} - F_{\mathrm{Bkg_1}} \qquad (5)$$

8

The determination of $F_{\mathrm{Bkg}_1}$ at supra-atmospheric conditions is difficult. As $P$ increases, the absorption features of NO broaden such that non-resonant wavelengths where the background signal can be directly measured, as done at ambient and low pressures [17], do not exist. Typically (*e.g.*, [13, 28]), $F_{\mathrm{Bkg}_1}$ is determined by taking measurements for a few levels of NO seeding in the reactants at on- and off-resonance wavelengths. For both values of $\lambda$, the change in the recorded signal with [NO] is approximated by a linear regression, and the background level taken as the signal at which the lines intercept. This method assumes that $F_{\mathrm{Bkg}_1}$ is identical at the on- and off-resonance wavelengths. However, the contribution of $O_2$-LIF interference rises with the pressure, and is wavelength dependent [27]. This inexact assumption could significantly impact the accuracy of the measurements for the current flames anticipated to produce very small amounts of NO.

An alternate background determination method, illustrated in Fig. 2, is proposed. Two excitation spectra are collected without (orange curve in Fig. 2) and with 53.7 ppm of NO injected in the reactant stream (green curve), a concentration expected to have a negligible effect on the flames [29]. Laser wavelengths from 226.005 to 226.115 nm are covered with a resolution of 1.375 picometres. At each station, 120 images are averaged, corrected for $S_{\mathrm{Bkg}_0}$, and normalized by $E_{\mathrm{L}}$. The measured excitation spectra with ($F_{\mathrm{exc,s}}$) and without ($F_{\mathrm{exc,u}}$) NO seeding can be expressed as:

$$F_{\mathrm{exc,s}}(\lambda) = F_{\mathrm{NO,s}}(\lambda) + F_{\mathrm{Bkg}_1}(\lambda), \tag{6}$$

and,

$$F_{\mathrm{exc,u}}(\lambda) = F_{\mathrm{NO,u}}(\lambda) + F_{\mathrm{Bkg}_1}(\lambda), \tag{7}$$

9

respectively. $F_{\mathrm{NO,u}}$ and $F_{\mathrm{NO,s}}$ are the excitation spectra, in the unseeded and seeded flames, of pure nitric oxide, and $F_{\mathrm{Bkg_1}}(\lambda)$ is the excitation spectrum of the interfering signal that does not depend on the NO concentration. Manipulating Eqs. (6) and (7) yields:

$$F_{\mathrm{Bkg_1}}(\lambda) = F_{\mathrm{exc,s}}(\lambda) - C_{\mathrm{Bkg}} \cdot \left[ F_{\mathrm{exc,s}}(\lambda) - F_{\mathrm{exc,u}}(\lambda) \right], \qquad (8)$$

where $F_{\mathrm{exc,s}}(\lambda) - F_{\mathrm{exc,u}}(\lambda) = F_{\mathrm{NO,s}}(\lambda) - F_{\mathrm{NO,u}}(\lambda)$ is the excitation spectrum of an arbitrary concentration of NO molecules (blue curve in Fig. 2), and $C_{\mathrm{Bkg}}$ is a variable independent of $\lambda$. The proper value of $C_{\mathrm{Bkg}}$ is sought that will provide an accurate description of $F_{\mathrm{Bkg_1}}(\lambda)$. However, Eq. (8) is an ill-resolved problem as both are unknown. Hence, an additional constraint is required, which does not assume that $F_{\mathrm{Bkg_1}}$ is independent of $\lambda$ as typically done [13, 28].

An iterative method is implemented that adjusts $C_{\mathrm{Bkg}}$ to minimize the least-squares difference between filtered and raw excitation spectra of $F_{\mathrm{Bkg_1}}$ calculated with Eq. (8) (Fig. 2 (b)-(d)). The argument is that, once the highly resonant NO excitation spectrum is completely subtracted of $F_{\mathrm{exc,s}}(\lambda)$, the relatively smooth $F_{\mathrm{Bkg_1}}(\lambda)$ trace (black curve) should match well with a filtered version of itself (grey curve), as shown in Fig. 2 (d). If an insufficient fraction of $F_{\mathrm{NO,s}}(\lambda) - F_{\mathrm{NO,u}}(\lambda)$ (blue curve) is deducted from $F_{\mathrm{exc,s}}(\lambda)$ (plot (b)), resonant NO features are still observed on the calculated background trace, and significant differences are observed between the raw (black) and filtered (grey) curves. Similarly, if a too large part of $F_{\mathrm{NO,s}}(\lambda) - F_{\mathrm{NO,u}}(\lambda)$ is subtracted of $F_{\mathrm{exc,s}}(\lambda)$ (plot (c)), reversed NO features are recognizable, and the fluorescence intensity may even reach negative values, which is non-physical. With this method, values of $C_{\mathrm{Bkg}}$ are computed for each axial

10

location (symbols in Fig. 3). Theory shows that the axial profile of $C_{\mathrm{Bkg}}$ should be a continuous function and, consequently, it is approximated by a sextic Bézier curve to reduce noise in the data. The axial profile of $F_{\mathrm{Bkg_1}}$ to be inserted in Eq. (5) is finally obtained by applying Eq. (8) at the excitation wavelength of $\sim 226.03$ nm, taking as inputs the Bézier curve approximation of $C_{\mathrm{Bkg}}$, and the averages of 5,000 images for $F_{\mathrm{exc,s}}$ and $F_{\mathrm{exc,u}}$.

Under weak laser irradiation, the NO-LIF signal can be described by Eq. (9), where $f_{\mathrm{LIF}}$ is the number of photons emitted per unit volume, $V$ [m$^3$], and laser energy; $N_{\mathrm{NO}}(T, P, X_{\mathrm{NO}})$ [m$^{-3}$] the number density of NO molecules; $f_{\mathrm{B}}(T)$ the Boltzmann fraction of NO molecules in the state excited by the laser; $\Delta\nu_{\mathrm{L}}$ [cm$^{-1}$] the spectral width of the laser; $\Gamma(\Delta\nu_{\mathrm{L}}, T, P, X_k)$ the dimensionless overlap fraction; $B_{12}$ [m$^2$J$^{-1}$s$^{-1}$] the Einstein constant of photon absorption; $A_{21}$ [s$^{-1}$] the rate constant of spontaneous emission; $Q_{21}(T, P, X_k)$ [s$^{-1}$] the rate constant of non-radiative collisional quenching; $\Omega$ [sr] the solid angle; $\tau_{\mathrm{opt}}$ the transmissivity of the collection optics; and $\epsilon$ [count / photon] the quantum efficiency of the camera.

$$\frac{S_{\mathrm{NO}}}{E_{\mathrm{L}}} = f_{\mathrm{LIF}}\left(N_{\mathrm{NO}}, f_{\mathrm{B}}, \lambda, \Delta\nu_{\mathrm{L}}, \Gamma, B_{12}, A_{21}, Q_{21}\right) \cdot \underbrace{\frac{\Omega}{4\pi} \cdot V \cdot \tau_{\mathrm{opt}} \cdot \epsilon}_{C_{\mathrm{opt}}} \qquad (9)$$

While $f_{\mathrm{LIF}}$ can be calculated by applying an appropriate model, here LIFSim [30], the optical parameters cannot be readily estimated, and the coefficient $C_{\mathrm{opt}}$ must be calibrated. Similar to Watson et al. [17, 18], the reactant stream is seeded with a known amount (53.7 ppm) of NO, and an axial profile of signal intensity at the on-resonance wavelength ($\left[S_{\mathrm{Raw}} - S_{\mathrm{Bkg_0}}\right]/E_{\mathrm{L}}$) is measured. A second profile without NO seeding is subtracted to remove the interfering signal ($F_{\mathrm{Bkg_1}}$), and the LIF intensity of the NO molecules produced
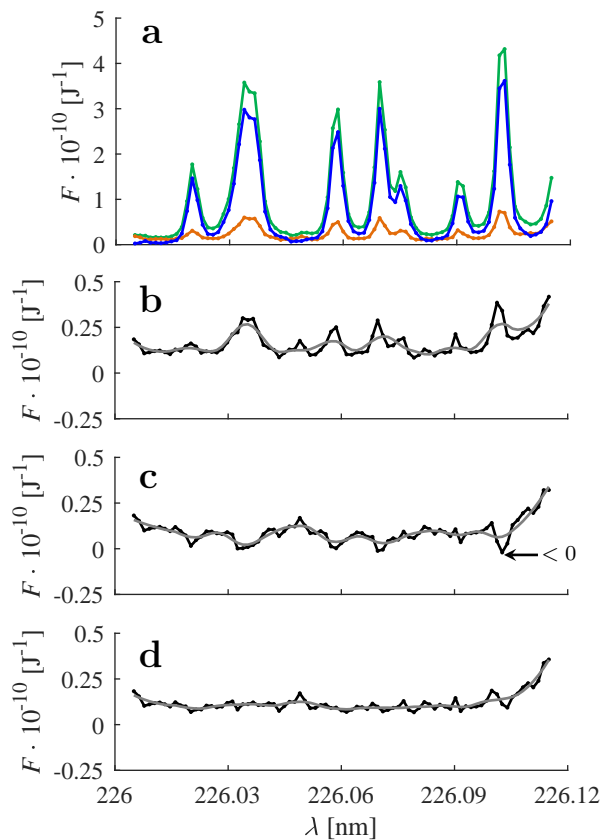
11

Figure 2: Iterative background determination method applied to the 2 atm flame at an axial position corresponding to pixel 50 (post-flame region) in Fig. 3. Plot (a) shows excitation spectra with ($F_{\mathrm{exc,s}}(\lambda)$, green) and without ($F_{\mathrm{exc,u}}(\lambda)$, orange) NO seeding, and for an arbitrary concentration of NO molecules ($F_{\mathrm{exc,s}}(\lambda) - F_{\mathrm{exc,u}}(\lambda)$, blue). Raw (black) and filtered (grey) excitation spectra of $F_{\mathrm{Bkg_1}}$ for $C_{\mathrm{Bkg}} = 1.1$ (b), $C_{\mathrm{Bkg}} = 1.2$ (c), and $C_{\mathrm{Bkg}} = 1.1634$ (d) (final solution).

12
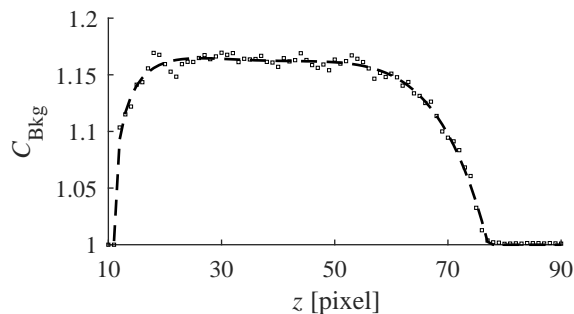
Figure 3: Axial profile of $C_{\mathrm{Bkg}}$. Legend: raw values (symbols), and least-squares adjusted sextic Bézier curve (dashed curve).

through the flame. This yields a NO-LIF profile corresponding to the seeded NO molecules only. The same procedure is reproduced numerically with Cantera and LIFSim. The experimental ($S_{\mathrm{NO}}/E_{\mathrm{L}}$) and numerical ($f_{\mathrm{LIF}}$) values are inserted in Eq. (9), and $C_{\mathrm{opt}}$ is adjusted to achieve the best agreement between both profiles. This methodology, repeated at each pressure, does not assume negligible NO consumption through the flame as the thermochemical model can, in theory, account for this phenomenon. However, NO reburn should be minimized to obtain the highest level of accuracy, which is expected for the lean flames presented in this work.

Typically, measured values of $S_{\mathrm{NO}}/E_{\mathrm{L}}$ are inserted in Eq. (9), and the LIF model is applied to extract an experimental number density of NO molecules. However, this method has drawbacks. It is necessary to hypothesize the temperature, pressure, and species concentration fields used in the LIF model, which induces uncertainties. Furthermore, if the LIF model is proven inadequate, it makes the experimental data obsolete even if the methodology was formally correct. Instead, as suggested by Connelly et al. [31], axial profiles of LIF intensity generated with LIFSim [30], based on flame simulations, are
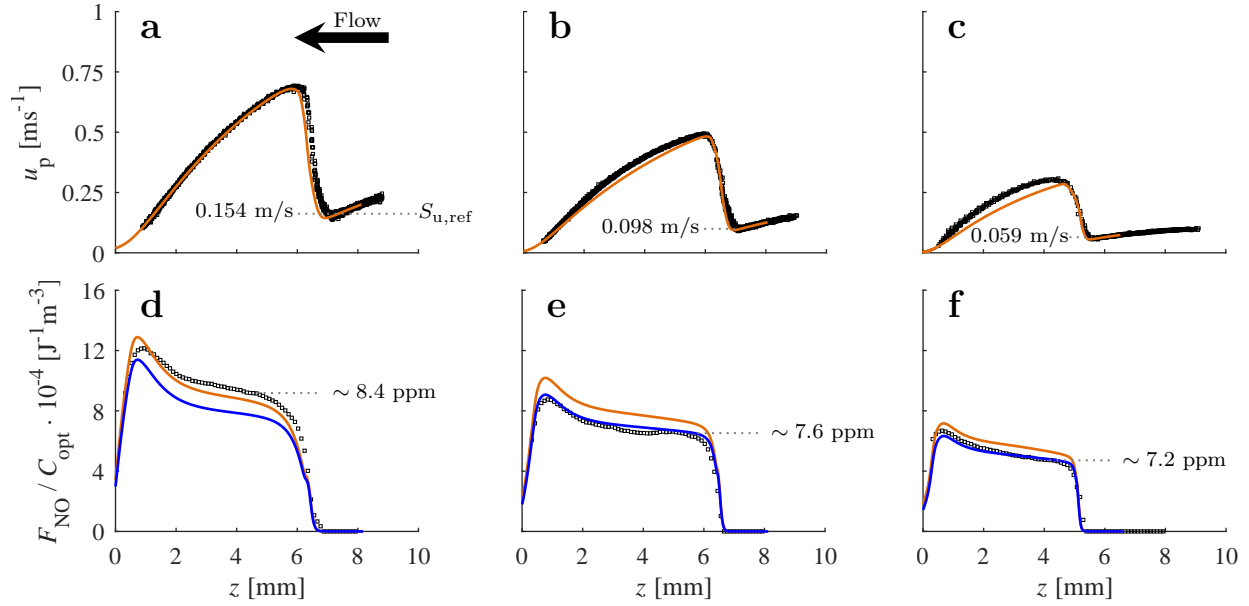
13

Figure 4: Profiles of axial particle velocity (top) and NO-LIF signal (bottom). $P = 2$ atm (first column), $P = 4$ atm (second column), and $P = 8$ atm (third column). The plate is located at $z = 0$ mm, and the outlet of the nozzle at $z \sim 9$ mm. Legend: experiments (symbols), NUIG (orange), NUIG with modified specific rate (blue). Only the NUIG model is shown in plots (a)-(c) as the predictions of both mechanisms exactly agree.

directly compared to the relatively raw experimental profiles.

## 4. Results and discussion

The experimental results are presented in Fig. 4. As expected, the flow initially decelerates, then rapidly accelerates through the flame front due to thermal expansion, and stagnates on the surface located at $z = 0$ mm (plots (a)-(c)). The strained, reference flame speed, $S_{u,ref}$, defined as the velocity minimum just upstream of the reaction zone, decreases with the pressure; a least-squares adjustment yields $S_{u,ref} \propto P^{-0.7}$.

14

Figure 4 (d)-(f) presents the NO-LIF intensity per unit laser energy normalized by $C_{opt}$ at 2, 4, and 8 atm. For all flames, the NO-LIF signal increases rapidly through the flame front, and then very slowly in the post-flame region. The rise and rapid decay of $F_{NO}/C_{opt}$ for $z \lesssim 2$ mm are attributed to the increase in the number density as the flow is cooled by the plate, and the consumption of nitric oxide, respectively. The weak rise of the LIF signal in the post-flame region not affected by heat loss to the surface indicates a slow rate of NO formation through the thermal (Zel'dovich) route, which is caused by the relatively low adiabatic flame temperature of $\sim 1835$ K for the three flames.

The predictions of a model recently assembled at the National University of Ireland, Galway (NUIG) [32, 33] are superimposed on the experimental data. For all cases, they agree very well with the velocity measurements of Fig. 4. A slight underestimation of the reference flame speed is noted, but the flame location is correctly captured. Unlike many other models, not presented here for the sake of brevity, the NUIG model predicts the proper magnitude of LIF intensity at all pressures. At 4 and 8 atm, the numerical NO-LIF signal in the post-flame region is overpredicted, which suggests that the rate of NO formation through the thermal route is overestimated. A recent investigation in atmospheric, premixed, stoichiometric, stagnation flames of alkanes and alcohols showed that the specific rate of the reaction $N_2 + O \leftrightarrow NO + N$, the initiation step of the thermal pathway, is overestimated in most thermochemical models [17], as well as in the collection of rate coefficients of Baulch et al. [34]. This finding is consistent with the specific rate recently provided in [35], and the results of the flow reactor

15

experiments reported in [36]. The specific rate suggested in [17] ($k(T) = 9.44 \cdot 10^{13} \cdot \exp\left(-38400/T\right)$ $\mathrm{cm^3/mol-s}$) was inserted in the NUIG mechanism. An almost perfect agreement of the simulations and experiments is observed at 4 and 8 atm, while the numerical data depart slightly more from the experimental values at 2 atm (blue curves in Fig. 4). The modified model is used in the remainder of this paper to study the effects of pressure on the NO chemistry.

Many parameters in Eq. (9) are affected by $P$, such that it is difficult to infer its impact on the formation of NO from the experimental LIF data of Fig. 4. The species and temperature profiles of the modified NUIG mechanism were inserted in LIFSim to estimate experimental NO mole fractions, immediately downstream of the flame front, of 8.4, 7.6, and 7.2 ppm at 2, 4, and 8 atm, respectively. Therefore, it is concluded that the pressure has only a very limited, negative impact on the formation of NO for the conditions considered in this study. Experiments were conducted at 16 atm, but interfering LIF completely masked the NO fluorescence signal, which could not be recovered. One-dimensional LIF with spectral resolution of the emission process to select more favourable NO emission bands is envisioned for future studies.

Reaction Pathway Analyses (RPA) [24] are used to identify the principal routes producing nitric oxide in the current flames. A cylindrical control volume (CV) is applied over the computational domain, and the flux of nitrogen atoms (a conserved scalar) transferred between the molecules as the reactants are transformed into products is calculated. A network similar to Fig. 5 is generated to quantify the fraction of the atoms initially in $N_2$ that
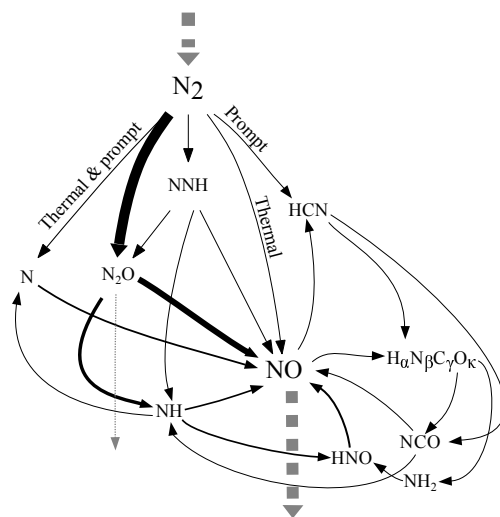
Figure 5: Reaction pathway analysis tracking the flux of nitrogen atoms in the 4 atm flame. The inlets of the RPA control volume and computational domain coincide, and the outlet of the CV, in this case, is placed at $z = 5$ mm. The dashed grey arrows indicate fluxes of N across the boundaries of the control volume. The nitrogen atoms leaving via the $N_2O$ molecules are deducted from the contribution of this route as they do not contribute to NO formation.
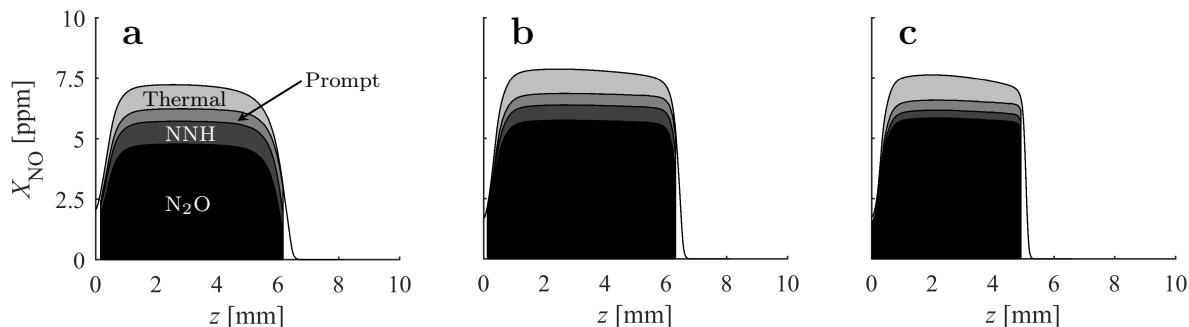


Figure 6: Predicted axial profiles of nitric oxide mole fraction. The contributions of each formation pathway are shown by the coloured areas. $P = 2$ atm (a), $P = 4$ atm (b), and $P = 8$ atm (c). Same legend for the three plots.

17

are introduced in each pathway. To prepare Fig. 6, the outlet of the CV is translated across the computational domain, and a RPA performed for each location.

At all pressures, the $N_2O$ pathway proceeds mostly through the flame front where its share of the total NO mole fraction ($X_{NO}$) increases rapidly. Interestingly, the amount of nitric oxide produced through this route is noticeably smaller at 2 atm. This suggests that the underprediction of the numerical LIF signal in Fig. 4 (d) could be solved by adjusting the pressure dependence of the $N_2O$ pathway. The NNH and prompt routes are also enabled in the flame front region by the presence of fuel fragments (H and CH), but their contribution remains limited as the concentration of these radicals is low for lean mixtures [19]. In the post-flame region not affected by heat loss to the plate, the predicted shallow rise in NO mole fraction is principally driven by the thermal route that progresses at a very slow rate due to the relatively low temperature of the gas and high activation energy of the initiation reaction. In this area, the NNH and prompt mechanisms are inactive as indicated by the constant width of their corresponding bands in Fig. 6, while the $N_2O$ pathway reacts very slowly.

As expected from the literature, the formation of NO through the $N_2O$ route rises for higher values of $P$ (the black region becomes taller). However, this effect appears very limited when considering the termolecular nature of the initiation reaction (1), and the fourfold increase in the pressure for the current experiments. Furthermore, the NNH and prompt routes are predicted to produce lesser amounts of nitric oxide as $P$ increases, such that the post-flame value of $X_{NO}$ does not change significantly, a behaviour that is also

18

observed experimentally.

## 5. Conclusion

This paper presents velocity and NO concentration measurements collected using particle tracking velocimetry and laser-induced fluorescence in lean, premixed, methane/air flames stabilized in a jet-wall burner at elevated pressures. In this configuration, the flame is hydrodynamically stabilized relatively far from the burner surfaces. This allows NO formation to be measured through the reaction zone, as well as in the post-flame region. The experimental data reveal that NO is rapidly formed through the flame front, and then rises very slowly due to the relatively low temperature of the products. NO mole fractions, immediately downstream of the flame front, of 8.4, 7.6, and 7.2 ppm at 2, 4, and 8 atm, respectively, were estimated from the experimental data. This demonstrates that the pressure has a very limited, negative impact on the production of nitric oxide in lean flames.

Predictions of the thermochemical mechanism recently published by the National University of Ireland, Galway were compared to the experiments. It was shown to adequately capture the flame speed and location, as well as the magnitude of the NO-LIF signal. The specific rate of the initiation reaction of the thermal pathway was adjusted to better describe NO production in the post-flame region at pressures of 4 and 8 atm. Reaction pathway analyses were applied to the solution of flame simulations made with this improved model to investigate the mechanisms of nitric oxide formation.

For all experimental conditions, the $N_2O$ pathway, proceeding mostly in the flame front region, is the dominant channel of NO formation. This route

19

yields slightly larger amounts of NO at higher pressures which, however, appears very limited when considering that its initiation reaction is termolecular, and that the pressure was quadrupled in the current experiments. In the post-flame region, the thermochemical model predicts a rise in the NO mole fraction mostly induced by the thermal route, while the NNH and prompt pathways, enabled in the reaction zone, only produce small quantities of NO. The contributions of these last two pathways are predicted to decrease with the pressure, thereby counteracting the strengthening of the $N_2O$ route. Consistent with the experiments, the formation of NO is observed not to significantly change with the pressure.

The measurements presented in this work can be used as accurate validation and optimization targets for the development of thermochemical mechanisms. The numerical values can be obtained from the authors.

## Acknowledgments

## References

[1] D. Vallero, Fundamentals of Air Pollution, Academic Press, $5^{th}$ edition, 2014.

[2] J. M. Bergthorson, M. J. Thomson, Renew. Sust. Energy Rev. 42 (2015) 1393–1417.

[3] A. H. Lefebvre, D. R. Ballal, Gas Turbine Combustion: Alternative Fuels and Emissions, CRC Press, 2010.

[4] T. C. Lieuwen, M. Chang, A. Amato, Combust. Flame 160 (2013) 1311–1314.

[5] A. C. A. Lipardi, P. Versailles, G. M. G. Watson, G. Bourque, J. M. Bergthorson, Combust. Flame 179 (2017) 325–337.

[6] A. M. Dean, J. W. Bozzelli, in: W. C. Gardiner Jr. (Ed.), Gas-phase combustion chemistry, Springer-Verlag, 2000, pp. 125–341.

[7] P. Gokulakrishnan, M. S. Klassen, in: T. C. Lieuwen, V. Yang (Eds.), Gas Turbine Emissions, Cambridge Edition, 2013, pp. 125–341.

[8] M. C. Drake, R. J. Blint, Combust. Sci. Technol. 75 (1991) 261–285.

[9] D. D. Thomsen, F. F. Kuligowski, N. M. Laurendeau, Combust. Flame 119 (1999) 307–318.

[10] J. R. Reisel, N. M. Laurendeau, Combust. Sci. Tech. 98 (1994) 137–160.

[11] J. R. Reisel, N. M. Laurendeau, Combust. Flame 101 (1995) 141–152.

[12] M. C. Drake, J. W. Ratcliffe, R. J. Blint, C. D. Carter, N. M. Laurendeau, Proc. Combust. Inst. 23 (1991) 387–395.

[13] L. Pillier, M. Idir, J. Molet, A. Matynia, S. De Persis, Fuel 150 (2015) 394–407.

[14] P. Versailles, A. Durocher, G. Bourque, J. M. Bergthorson, in: Proc. ASME Turbo Expo 2018, Oslo, Norway. GT2018-77018.

21

[15] J. M. Bergthorson, D. G. Goodwin, P. E. Dimotakis, Proc. Combust. Inst. 30 (2005) 1637–1644.

[16] J. M. Bergthorson, P. E. Dimotakis, Proc. Combust. Inst. 31 (2007) 1139–1147.

[17] G. M. G. Watson, P. Versailles, J. M. Bergthorson, Combust. Flame 169 (2016) 242–260.

[18] G. M. G. Watson, P. Versailles, J. M. Bergthorson, Proc. Combust. Inst. 36 (2017) 627–635.

[19] P. Versailles, G. M. G. Watson, A. C. A. Lipardi, J. M. Bergthorson, Combust. Flame 165 (2016) 109–124.

[20] P. Versailles, J. M. Bergthorson, J. Fluids Eng. 134 (2012).

[21] R. J. Kee, J. A. Miller, G. H. Evans, G. Dixon-Lewis, Proc. Combust. Inst. 22 (1989) 1479–1494.

[22] D. G. Goodwin, H. K. Moffat, R. L. Speth, Cantera: An object-oriented software toolkit for chemical kinetics, thermodynamics, and transport processes, 2017. Version 2.3, http://www.cantera.org.

[23] J. M. Bergthorson, S. D. Salusbury, P. E. Dimotakis, J. Fluid Mech. 681 (2011) 340—-369.

[24] P. Versailles, CH formation in premixed flames of $C_1$–$C_4$ alkanes: assessment of current chemical modelling capability against experiments, Ph.D. thesis, McGill University, 2017. http://digitool.library.mcgill.ca/R/.

[25] J. M. Bergthorson, P. E. Dimotakis, Exp. Fluids 41 (2006) 255–263.

[26] M. D. DiRosa, K. G. Klavuhn, R. K. Hanson, Combust. Sci. Technol. 118 (1996) 257–283.

[27] W. G. Bessler, C. Schulz, T. Lee, J. B. Jeffries, R. K. Hanson, Appl. Opt. 42 (2003) 4922–4936.

[28] D. D. Thomsen, F. F. Kuligowski, N. M. Laurendeau, Appl. Opt. 36 (1997) 3244–3252.

[29] W. G. Bessler, C. Schulz, T. Lee, D. I. Shin, M. Hofmann, J. B. Jeffries, J. Wolfrum, R. K. Hanson, Appl. Phys. B 75 (2002) 97–102.

[30] W. G. Bessler, V. Sick, J. W. Daily, Proc. 3rd Joint Meeting, U.S. Sections of the Combust. Inst. 105 (2003) 1–6.

[31] B. C. Connelly, B. A. V. Bennett, M. D. Smooke, M. B. Long, Proc. Combust. Inst. 32 (2009) 879–886.

[32] C. W. Zhou, Y. Li, E. O'Connor, K. P. Somers, S. Thion, C. Keesee, O. Mathieu, E. L. Petersen, T. A. DeVerter, M. A. Oehlschlaeger, G. Kukkadapu, C. J. Sung, M. Alrefae, F. Khaled, A. Farooq, P. Dirrenberger, P. A. Glaude, F. Battin-Leclerc, J. Santner, Y. Ju, T. Held, F. M. Haas, F. L. Dryer, H. J. Curran, Combust. Flame 167 (2016) 353–379.

[33] Y. Zhang, O. Mathieu, E. L. Petersen, G. Bourque, H. J. Curran, Combust. Flame 182 (2017) 122–141.

[34] D. L. Baulch, C. J. Cobos, C. T. Bowman, R. A. Cox, J Phys. Chem Ref. Data 34 (2005) 757–1397.

[35] N. Lamoureux, H. El Merhubi, L. Pillier, S. de Persis, , P. Desgroux, Combust. Flame 163 (2016) 557–575.

[36] M. Abian, M. U. Alzueta, P. Glarborg, Int. J. Chem. Kin. 47 (2015) 518–532.

## Supplemental material

The file *Versailles_HP_NOx_SuppMaterial.pdf* contains the boundary conditions required for the flame simulations.